Journal Article

Phosphorylated Salmon bone polypeptides: enhancing stability and antimicrobial activity through zinc chelation

Han L, Dong N, Hu B, Yang J, Jiao Z, Ma K, Xu Z and Li T

Food Chemistry: X 32 (2025) 103350

Contents lists available at ScienceDirect

Food Chemistry: X

journal homepage: www.sciencedirect.com/journal/food-chemistry-x

Phosphorylated Salmon bone polypeptides: enhancing stability and antimicrobial activity through zinc chelation

Lingyu Han [a,1], Nuo Dong [a,1], Bing Hu [a], Jixin Yang [b], Zhiwei Jiao [a], Kun Ma [a], Zhe Xu [a], Tingting Li [a,*]

[a] Key Lab of Biotechnology and Bioresources Utilization of Ministry of Education, College of Life Science, Dalian Minzu University, Dalian, Liaoning 116600, China
[b] Faculty of Arts, Science and Technology, Wrexham University, Plas Coch, Mold Road, Wrexham LL11 2AW, United Kingdom

ARTICLE INFO

Keywords:
Salmon bone peptide
Phosphorylation reactions
Simulated gastrointestinal digestion
Antimicrobial

ABSTRACT

Salmon bones, a marine waste, have bioactive potential. Salmon bone peptides (SBPs) were phosphorylated at different pH to form P-SBPs, whose structure and that of their zinc chelates (P-SBPs-Zn) were analyzed *via* Fourier-transform infrared spectroscopy, fluorescence spectroscopy and CD spectrum. Among the pH-modified variants, phosphopeptide-zinc chelates at pH 4 (P-SBPs4-Zn) exhibited the best solubility and highest zinc chelating property, with a zinc content of 86.15 ± 0.47 mg/g. The stability and digestibility were tested under simulated gastrointestinal conditions (adults/elderly, dietary components). P-SBPs4-Zn demonstrated optimal stability and digestibility. After evaluation the antibacterial activity, P-SBPs4-Zn exhibited significant antibacterial effects against *Escherichia coli* and *Staphylococcus aureus* through mechanisms involving membrane disruption. The safety assessment using Caco-2 and RAW 264.7 cells confirmed its biocompatibility, supporting its suitability for oral application. This supports its use as an efficient, stable, antibacterial zinc supplement for food processing.

1. Introduction

Zinc, often referred to as the “life element”, plays a crucial role in maintaining essential physiological functions and supporting overall human health. Zinc deficiency is associated with several health risks: in children, it can impair growth and development; while in adults, it can damage gonadal function and lead to neurological dysfunction and compromised immunity (Wang et al., 2012). Zinc intake can be increased through zinc-rich foods or through zinc supplements. Currently, four primary forms of zinc supplements are available: those synthesized with inorganic zinc salts, organic weak acids, amino acids, and peptides as ligands (Salami et al., 2016). Food-derived peptides have shown potential as zinc carriers due to their chelating abilities (Udechukwu et al., 2016). Some peptide structures, containing amino acids such as His, Cys, Asp, Glu, and Ser, can form soluble zinc chelates, thereby enhancing zinc absorption and preventing it from binding with phytates. Zinc chelates, formed through the binding of zinc ions with the C-terminal carboxyl group, N-terminal amino group, amino acid side chains, imino, and carbonyl group in peptide chains, offer high bioavailability, bioactivity, solubility, and safety. These characteristics make peptide-zinc chelates a promising area of research, with studies reporting their effectiveness in inhibiting bacterial growth, while being less toxic to humans (Fang et al., 2019) Although the structure and intestinal absorption of peptide-zinc chelate have been investigated, limited studies have explored their gastrointestinal digestibility, antimicrobial mechanisms and effects in elderly populations.

Salmon bone, a byproduct of seafood processing, is increasingly acknowledged as a sustainable source of bioactive components. Recent studies indicate that enzymatic hydrolysis of salmon bone proteins yields salmon bone peptide (SBPs), which exhibit significantly enhanced bioactivity relative to their native protein precursors. Documented multifunctional properties of SBPs include strong metal chelation capacity, immunomodulatory effects, and therapeutic potential against chronic conditions like hypertension and hypercholesterolemia (Ma et al., 2017). Notably, their antimicrobial and antioxidant activities indicate promising applications in food preservation and nutraceutical development. Of particular relevance to this study, the phosphorylatable serine residues in SBPs offer unique opportunities for structural

* Corresponding author.
E-mail address: jwltt@dlnu.edu.cn (T. Li).
[1] The authors contributed equally to this work.

https://doi.org/10.1016/j.fochx.2025.103350
Received 18 June 2025; Received in revised form 26 November 2025; Accepted 28 November 2025
Available online 30 November 2025

modification, enabling the design of tailored peptide-zinc complexes with enhanced stability and functionality. These advancements establish SBPs as a compelling subject for exploring the interplay between peptide modification, mineral chelation, and biological efficacy in food-derived bioactive systems. Phosphorylation modification increases the number of charges on the peptide chain and improves the solubility of the peptide in water. By altering the spatial structure of peptide, a more stable conformation is resulted in, which enhances the stability of peptide against factors such as enzymatic degradation, acidic and alkaline environments, and heat (Quan et al., 2019). Accordingly, we propose the hypothesis that phosphorylation modification of SBPs could enhance their zinc chelation capacity by promoting structural stabilization. This would improve zinc bioavailability during gastrointestinal digestion. Additionally, this modification may enable the peptide molecules to interact more effectively with bacterial cell membranes, thereby exerting antibacterial effects. Its dual functionality may diminish the requirement for separate preservatives, thereby reducing overall formulation costs.

In this study, SBPs were prepared using neutral protease enzymolysis of salmon bone. The molecular weight of these peptides was analyzed through liquid chromatography. Salmon bone phosphopeptides (P-SBPs) with varying pH values (pH 3–9) were then prepared to study the effects of phosphorylation. The structure and properties of P-SBPs were characterized through infrared spectroscopy, circular dichroism (CD), fluorescence, surface hydrophobicity, and phosphorylation degree. Additionally, the zinc-binding capability of the P-SBPs zinc chelate (P-SBPs-Zn) was evaluated through elemental composition, CD spectrum, and zinc content analyses, alongside assessments of the chelate's stability to determine the optimal product. Finally, the antibacterial properties of P-SBPs4-Zn were examined. This study aims to prepare phosphorylated salmon bone polypeptides (P-SBPs), characterize the formation and structural properties of P-SBPs-zinc chelates, evaluate the effect of zinc chelation on the stability of P-SBPs as well as the antibacterial activity of P-SBPs-Zn against common foodborne pathogenic bacteria, and clarify the potential mechanism underlying the enhanced stability and antibacterial performance of P-SBPs-Zn. The findings of this research are expected to provide a theoretical basis for the development of P-SBPs-Zn as a functional material for food preservation or zinc-rich food products, while also facilitating the high-value utilization of salmon processing by-products.

2. Materials and methods

2.1. Materials

Salmon bones were sourced from Dalian Sea Treasure Breeding Co. Ltd. in Jinzhou, China, and neutral protease (60,000 U/g) was obtained from Solarbio (Shanghai, China). Aprotinin hydrochloride (high-purity, 6000 U/mg), β-amyloid (HPLC, ≥95 %), cyanocobalamin (HPLC, ≥99 %), oxalate (Analytically pure, 98 %), phytic acid (Biological Reagent, 70 %) and fusayama (pH 7.0) were purchased from Yuanye Bio-Technology Co. Ltd. (Shanghai, China). Sodium tripolyphosphate (STPP) and cytochrome C (HPLC, ≥95 %) were obtained from Aladdin Reagent Co. Ltd. (Shanghai, China). Zinc gluconate and $ZnSO_4{\cdot}7H_2O$ were obtained from Macklin Reagent Co. Ltd. (Shanghai, China). The RAW 264.7 cell line and Caco-2 cell line were obtained from the Cell Bank of the Chinese Academy of Sciences (Shanghai, China). All other chemicals and reagents used in this study were of analytical grade. The study utilized *Escherichia coli* and *Staphylococcus aureus* bacteria from China Agricultural Microbial Strain Collection Management Center.

2.2. Preparation of SBPs

In order to extract water-soluble protein from salmon bones, they were mixed with deionized water (1:3 *w*/w), homogenized for 5 min, and the resulting slurry was centrifuged at 4 °C at 9700 r/m for 10 min (Han et al., 2024). The supernatant was collected and freeze dried to obtain fish bone protein powder, which was used to prepare SBPs. The water-soluble fish bone protein was dissolved in deionized water (1:50) and hydrolyzed by a neutral protease (50 °C, pH 7.0) at a dose of 5000 U/g protein. After 5 h of reaction, the solution was heated to 100 °C for 10 min to inactivate the enzyme. The resulting mixture was centrifuged at 9700 r/m for 10 min, and the supernatant was freeze dried and stored at −18 °C until use.

2.3. Molecular weight distribution of SBPs

The sample was prepared with a mass concentration of 1 mg/mL and filtered through a 0.45 μm membrane. Molecular weight was determined using a 1200 liquid chromatograph (Agilent Technologies, Inc., USA).The mobile phase consisted of acetonitrile, water, and trifluoroacetic acid in a ratio of 30:70:0.1 (*v*/v/v), with a flow rate set at 0.8 mL/min. Molecular weight calibration curves were established using standards including cytochrome C (12,500 Da), aprotinin hydrochloride (6512 Da), β-amyloid (4514 Da) and cyanocobalamin (1355 Da). First, measure the retention times of these four standard substances under the same chromatographic conditions, and then fit a linear regression model between the logarithm of the molecular weight and the retention time. The formula was $y = -0.0008x + 16.384$, $R^2 = 0.9953$ (Supplementary Fig. 1). The molecular weight of SBPs is calculated by substituting the retention time determined by it into the standard curve.

2.4. Preparation of P-SBPs at different pH values

Xiong and Ma (2017) described the dry-heat method for obtaining phosphorylated SBPs (P-SBPs). In this study, SBPs were dissolved in a sodium tripolyphosphate solution with a concentration of 20 g/L. The pH of the mixture was adjusted to 3.0, 4.0, 5.0, 6.0, 7.0, 8.0 and 9.0 using either a 1 M solution of either HCl or NaOH accordingly and then freeze-dried in an FD-1A-50+ freeze-dryer (BIOCOOL, Beijing, China). The powder was incubated at a temperature of 45 °C and a relative humidity of 79 % for 12 h in an SPX-150B-Z incubator (Shanghai, China). The products were dialyzed in deionized water for 48 h to remove unbound phosphate ions. The phosphorylated products from the aqueous suspension were named P-SBPs3, P-SBPs4, P-SBPs5, P-SBPs6, P-SBPs7, P-SBPs8, and P-SBPs9 according to their respective preparation pH values. They were stored in a sealed container at −20 °C for future use.

2.5. Structural characterization of P-SBPs at different pH values

2.5.1. Fourier-transform infrared spectroscopy (FT-IR)

Adapted according to the method of Chen et al. (2024). The three mg sample powder and 300 mg potassium bromide were respectively weighed and ground in a mortar by using the KBr tablet method. The measurement was performed by using IRPrestige21 spectrometer (Shimadzu, Japan). The scanning parameters were as follows: spectral range 4000–500 cm^{-1}, No. of scans 30, and the scanning speed 0.2 cm/s.

2.5.2. CD Spectrum

According to the method of Zhu et al. (2021), the secondary structure of the product was determined by circular dichroism spectrometry (Chirascan V100, Applied Photophysics, Leatherhead, Surrey, UK). Under the premise of satisfying the test voltage, the mass concentration of the sample to be measured is formulated as 1.0 mg/mL. The CDNN software simultaneously analyzed the secondary structure of each sample three times. Each sample was examined between 190 and 260 nm at a scanning speed of 100 nm/min, with a response time of 0.25 s.

2.5.3. Fluorescence spectral analysis

The fluorescence spectra of SBPs (dissolved in ultrapure water, 1 mg/mL) at various pH values were determined by a Perkin Elmer LS-55

fluorescence spectrometer (USA). The excitation wavelength is 290 nm and the emission wavelength ranged from 300 to 500 nm.

2.5.4. Surface hydrophobicity (H_0) determination

The method was adapted from Luo et al. (2022) and slightly modified where fluorescent probe technology was employed. First, the sample was diluted to a series of mass concentration gradients, including 0.0125, 0.025, 0.05, 0.1, and 0.2 mg/mL, dissolved in a 0.02 mol/L phosphate buffer at pH 7. Each 5 mL sample solution contained 0.2 μmol ANS fluorescent probe (1-aniline-8-naphthalene sulfonic acid). The fluorescence intensity of the solution was measured using a fluorescence spectrophotometer with an excitation wavelength of 290 nm and an emission wavelength range of 300–500 nm. Three parallel experiments were conducted for each group of samples, and the results were averaged. The obtained fluorescence intensity data and corresponding protein mass concentration (mg/mL) were subjected to linear regression analysis. The resulting slope of the linear regression represents the surface hydrophobicity, which provides insights into the number and characteristics of hydrophobic regions on protein molecules.

2.5.5. Phosphorylation assay

The level of phosphorylation was assessed utilizing a phosphorylation assay kit from Elabscience Biotechnology *Co. Ltd* (*E*-BC-K245-M, Wuhan, China) through the calculation with the following formula.

$$Pi\left(\frac{mmol}{L}\right) = (\Delta A_{660} - b) \div a \times 5 \times f \quad (1)$$

where ΔA_{660} is sample absorbance - blank absorbance, b is the intercept, a is the slope of the standard curve and f is the dilution ratio of the sample.

2.6. Preparation of P-SBPs-Zn at different pH values

Adapting to the method proposed by Sun et al. (2021), P-SBPs with varying pH values were combined with a 5 mmol/L zinc sulfate solution at a mass ratio of 3:1. The reaction was conducted at 40 °C in a temperature-controlled water bath for 30 min. Subsequently, anhydrous ethanol was added to the reaction mixture at a volume ratio of 1:3 (water phase: ethanol) to precipitate the salmon bone phosphopeptide zinc chelate (P-SBPs-Zn). After centrifugation at 6860 r/m for 5 min, the supernatant was discarded, and the sediment was collected and freeze-dried for future use.

2.7. Determination of the chelating ability of P-SBPs-Zn

The zinc content was determined by kit (Nanjing Jiancheng Bioengineering Research Institute, China). Tris buffer (100 mmol/L), zinc-mercury (7 mmol/L) and the sample to be tested (1 mg/mL) were added at 10:1:1 (*v*/v). After incubating at 37 °C for 5 min the absorbance was measured at 630 nm. Zinc content was calculated according to the following formula.

$$\text{Zinc ion concentration } (\mu mol/L) = C_{\text{standard}} \times \frac{A_{measure}}{A_{standard}} \quad (2)$$

$$\text{Zincchelatingability}(mg/g) = \frac{\text{Zincionconcentration}(mmol/L) \times 1000 \times M}{Total concentration of zincions (mmol/L) \times M} \quad (3)$$

where C_{standard} is 24, $A_{measure}$ is the absorbance of the sample and $A_{standard}$ is the absorbance of the standard.

2.8. Structural characterization of P-SBPs-Zn

2.8.1. Fourier-transform infrared spectroscopy (FT-IR)

Weigh out equal amounts of sample powder and potassium bromide (1:100, *w*/w) and grind them in a mortar using the potassium bromide tableting method. Measurements were performed using an IRPrestige21 spectrometer (Shimadzu, Japan). The scanning parameters were as follows: spectral range 4000–500 cm^{-1}, 30 scans, and a scan speed of 0.2 cm/s.

2.8.2. CD Spectrum

The mass concentration of the sample to be measured was 1.0 mg/mL. The spectrum scanning range was set to 190–260 nm, the scanning speed was 100 nm/min, and the response time was 0.25 s. The secondary structure of the sample was analyzed by CDNN software. Each sample was tested in parallel 3 times.

2.8.3. Fluorescence spectral analysis

The fluorescence spectrum of P-SBPs-Zn (1 mg/mL) at different pH values was measured using a PerkinElmer LS-55 fluorescence spectrometer. The excitation wavelength was 290 nm, and the emission wavelength range was 300 to 500 nm.

2.8.4. Elemental composition analysis

The microstructure and surface elements of SBPs, P-SBPs4, and P-SBPs4-Zn were observed by a scanning electron microscope (SEM, S4800, Hitachi, Tokyo, Japan) equipped with an energy dispersive spectrometer. The samples were coated with Au-Pd at a current of 15 mA for 90 s. The samples were imaged at a voltage of 5 kV with 3000× magnification.

2.9. Stability analysis of P-SBPs-Zn

2.9.1. Effects of glucose and NaCl treatments

The stability of adding different concentrations of glucose and NaCl was measured according to Zheng et al. (2023). Different amounts of glucose were added to P-SBPs-Zn solutions (1 mg/mL) at different pH values with final concentrations of 4, 8 and 12 g/100 g, respectively. After stirring at 65 °C and 115 rpm for 20 min, the mixture was centrifuged at 6140 r/m for 12 min and the supernatant was combined. The zinc solubility was calculated using Eq. (4). The same systems were prepared with NaCl (1, 2 and 4 g/100 g) instead of glucose to study the effect of NaCl on the solubility of zinc in P-SBPs-Zn solutions at different pH values. Zinc gluconate (100 μg/mL) were used as comparisons.

$$\text{Zinc solubility } (\%) = \text{Zinc in supernatant/Total zinc in solution} \times 100 \quad (4)$$

2.9.2. Simulation of the effects of gastrointestinal digestion in adults

The *in vitro* digestion process of P-SBPs-Zn at different pH values was studied using an oral gastrointestinal digestion method (based on the method reported by Yu et al. (2024) and Feng et al. (2024) with minor modifications). First, the sample solution (1 mg/mL) was mixed with an equal volume (7.5 mL) of simulated saliva, adjusted to pH 6.8, and incubated at 37 °C and 150 rpm for 5 min. Subsequently, 15 mL of simulated gastric fluid (containing 3.2 g/L pepsin and 2 g/L NaCl) was added, and the pH was adjusted to 2. Incubation continued at 37 °C and 120 rpm for 120 min. Finally, 7.5 mL of simulated intestinal fluid was added, the pH was adjusted to 7, and incubation continued at 37 °C and 130 rpm for 120 min. The simulated intestinal fluid formulation was as follows: 1.5 mL salt solution (100 μM $ZnSO_4$, 1.67 mM $CaCl_2$), 2.5 mL enzyme solution (60 mg/mL phosphatase-buffered trypsin, 60 mg/mL phosphatase-buffered lipase), 3.5 mL 187.5 mg/mL phosphate-buffered

bile salt solution. After centrifugation for 10 min (6000 rpm), the fluorescence intensity of each digested sample was measured. The control group used zinc gluconate.

Additionally, food co-existing components (oxalic acid and phytic acid) were incorporated into the experiments. Methods were adapted from Feng et al. (2024) with minor modifications. *In vitro* digestion experiments included 0.61 mM phytic acid and oxalic acid. This ratio was selected to provide a standardized, direct comparative assessment for evaluating chelation competition between P-SBPs4-Zn and each inhibitor under simplified *in vitro* conditions. When analyzing the effects of food co-existing components on zinc solubility, the group without added components served as the control. Zinc solubility was calculated using Eq. (4).

2.9.3. Simulation of the effects of gastrointestinal digestion in the elderly

The elderly digestive model is based on differences in gastrointestinal digestive pH, digestive fluid (enzyme/substrate ratio), and peristaltic velocity (magnetic stirring velocity) (Hernández-Olivas et al., 2020). 7.5 mL of a 1 mg/mL sample solution was mixed with an equal volume of simulated saliva at pH 7.0, followed by incubation at 37 °C and 120 rpm for 5 min. Subsequently, 15 mL of simulated gastric fluid (containing 1.6 g/L pepsin and 2 g/L NaCl) was added to the system with pH adjusted to 2.5, followed by incubation at 37 °C and 100 rpm for 120 min. Finally, 7.5 mL simulated intestinal fluid was added with pH adjusted to 7.2, followed by incubation at 37 °C and 110 rpm for 120 min. The simulated intestinal fluid formulation is as follows: 1.5 mL salt solution (100 μM $ZnSO_4$, 1.67 mM $CaCl_2$), 2.5 mL each of 30 mg/mL phosphate-buffered trypsin and lipase, and 3.5 mL of 93.75 mg/mL phosphate-buffered bile salts. After digestion, centrifuge the mixture at 6000 rpm for 10 min and measure the fluorescence intensity of the resulting supernatant (digest). Zinc gluconate served as the control in this experiment.

To evaluate the effect of food co-ingested components on zinc solubility in the elderly, we added 0.61 mM oxalic acid and phytic acid to an *in vitro* simulated digestive system. Samples without added co-ingested food components served as blank controls for this analysis. Zinc solubility in each group was calculated using formula (4) described earlier in this paper.

2.10. Antimicrobial activity of P-SBPs-Zn

2.10.1. Oxford cup method assay

The inhibitory activity of P-SBPs4-Zn against *Escherichia coli (E. coli) and Staphylococcus aureus (S. aureus)* was determined by a slightly modified Oxford cup method. Bacteria cultured overnight were inoculated in LB petri dishes (Wang et al., 2019). After the medium had solidified, the sterile Oxford cup was removed. 200 μL (100 mg/mL) of sample solution and the same amount of zinc salt were added to the Oxford cup. 0.2 % streptomycin and potassium sorbate were used as positive control, with sterile water being negative control. After incubation at 37 °C and 25 °C, inhibition zone diameter (including disc area) was measured with a digital caliper to assess inhibition activity and recorded in millimeters. These values were described as the mean ± standard deviation of three simulated rows.

2.10.2. Minimum inhibitory concentration (MIC)

The MIC assay was adapted from a previously reported method (Shi et al., 2017) with slight modifications using 96-well microtitre cell culture plates prepared with 50 μL LB (10^7 CFU/mL) in each well, followed by transfer of the sample solution to broth and incubation at 37 °C for 12 h. The absorbance of each hole at 600 nm was measured by a microdrop plate instrument. The final concentrations were 40, 20, 10, 5, 2.5, 1.25, 0.63, 0.31 mg/mL without *E. coli* and 30, 15, 7.5, 3.75, 1.88, 0.94, 0.47, 0.23 mg/mL without *S. aureus* inoculation. The MIC value is defined as the minimum P-SBPs4-Zn concentration that inhibits microbial growth, where the antibacterial activity of P-SBPs4-Zn was evaluated using the unit mg/mL.

2.11. Antibacterial mechanism of P-SBPs4-Zn

2.11.1. Scanning electron microscope (SEM)

The SEM analysis was performed according to the method reported by Bajpai et al. (2013) with slight modification. The samples to be tested were added to the log-phase *E. coli* and *S. aureus* resuspensions washed twice with 0.1 M phosphate buffer solution (PBS, pH 7.4), respectively. Bacterial cells were prepared by centrifugation and incubated at 37 °C for 8 h. Observations were made using an S-4800 scanning electron microscope (Hitachi Ltd., Japan). Scanning electron microscopy analysis was performed using the method of Diao et al. (2014).

2.11.2. Cell membrane integrity

Bacteria were cultivated in liquid medium to logarithmic growth phase. An appropriate amount of bacterial solution was centrifuged at 9700 r/m for 5 min at room temperature. After discarding the supernatant, it was washed with saline (ST341) once, and the concentration of the bacterial solution was adjusted to about 10^8 bacteria/ml ($OD_{670} \approx 0.3$) with saline. For every 100 μL of bacterial solution, 1 μL of staining work solution was added and thoroughly mixed before incubation at 37 °C for 30 min away from light. Then, 10 μL of the bacterial solution was added onto an adhesion slide (FSL051, Beyotime, China, with positively charged surface) and covered with a 24 mm square coverslip (FCGF24, Beyotime, China), and the staining was observed under a laser scanning fluorescence microscope FLUOVIEW FV3000 (OLYMPUS, USA). DMAO is green fluorescence, Ex/Em = 503/530 nm; PI is red fluorescence, Ex/Em = 535/617 nm.

2.11.3. Nucleic acid and protein leakage

The cell integrity detection methods of *E. coli* and *S. aureus* strains were adapted from Lv et al. (2011) with slight modification. At 37 °C, the cell suspension was incubated and stirred in two solutions of different concentrations (control and MIC). Samples collected (10 mL) every hour were centrifuged at 8000 rpm for 8 min to obtain supernatant, and sterile water was used as control group. The concentration of nucleic acid in the supernatant was determined using an ultraviolet-visible spectrophotometer (UV-2450, Shimadzu, Japan) by measuring the absorbance at a wavelength of 260 nm. In addition, the content of proteins in suspension was measured following the method of Xu et al. (2010).

2.12. In vitro cytotoxicity assay

2.12.1. RAW 264.7 cells

The potential cytotoxicity of P-SBPs4-Zn on RAW 264.7 cells was assessed by MTT assay. First, RAW 264.7 cells in DMEM complete medium (including 1 % penicillin-streptomycin and 10 % FBS) were inoculated into 96-well plates at a density of 1×10^4 cells per well. They were incubated for 24 h under standard conditions. Subsequently, the medium was replaced with the ones containing samples at different concentrations (0, 0.25, 0.5, 0.75, 1, and 1.25 mg/mL). After another 24 h of incubation, 20 μL of PBS solution of MTT reagent (5 mg/mL) was added to each well and the plates were incubated for 4 h. The solution was then removed and 150 μL of DMSO was added to each well. Absorbance was measured at 490 nm using a Synergy H1 enzyme labeler (BioTek, USA). Cell viability was calculated using Eq. (5):

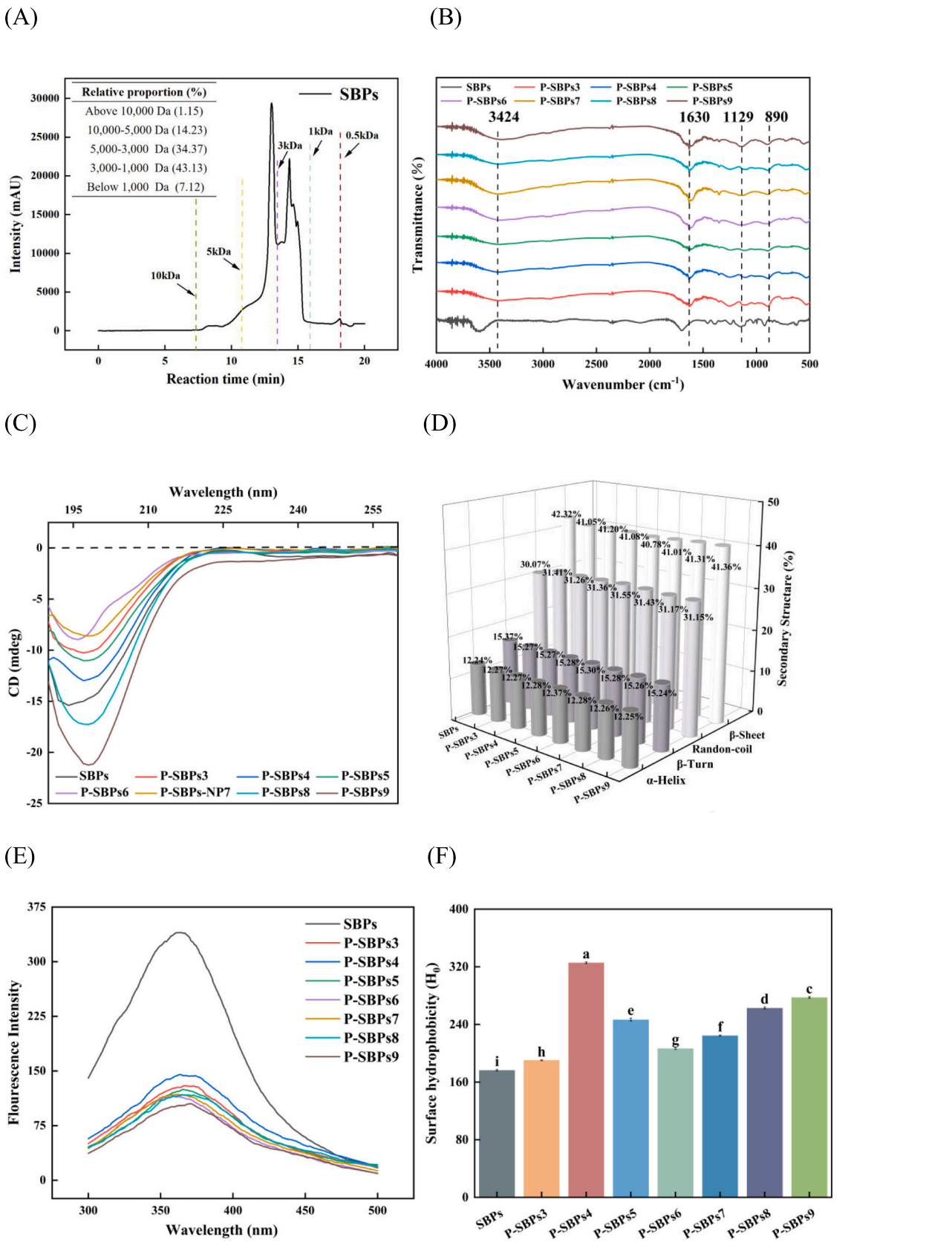

Fig. 1. Characterizations of SBPs and P-SBPs. (A) Molecular mass distribution of SBPs. (B) FT-IR spectra; (C) circular dichroic spectra; (D) secondary structure distribution; (E) fluorescence spectra; (F) surface hydrophobicity; (G) degree of phosphorylation and (H) zinc content of P-SBPs at varying pH values.

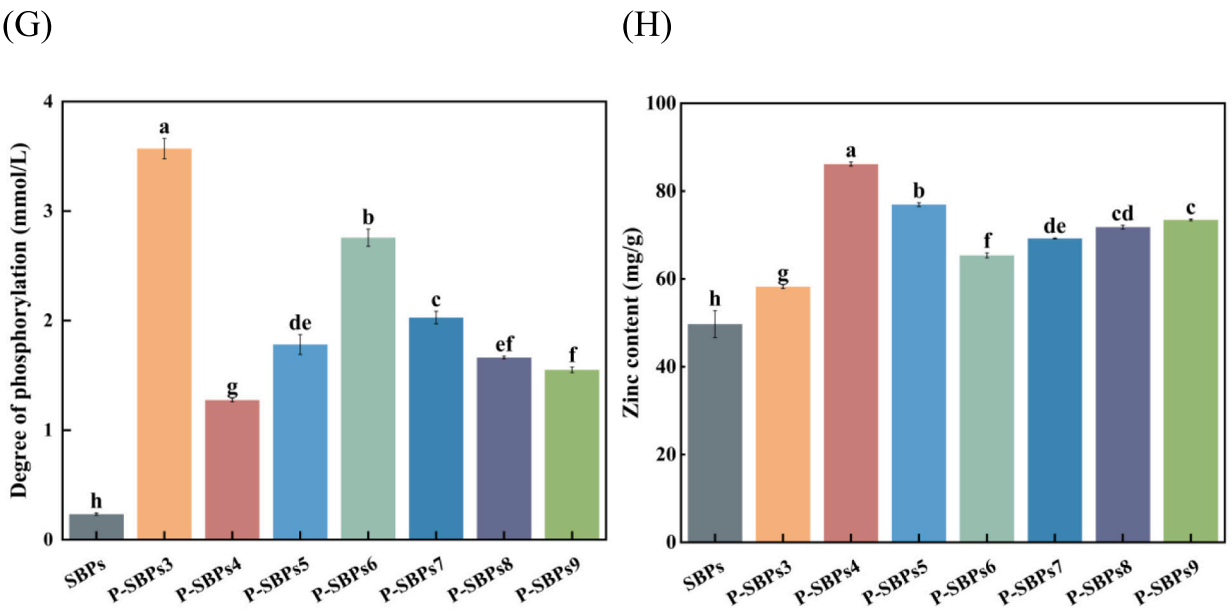

Fig. 1. (*continued*).

$$100\%\text{Cell viability} = \frac{At - Ac}{Au - Ac} \quad (5)$$

where At and Au represent absorbances at 490 nm in the presence and absence of sample, respectively; Ac is the absorbance of the control with no cells.

2.12.2. Caco-2 cells

To assess the potential cytotoxicity of P-SBPs4-Zn on intestinal epithelial cells, Caco-2 cells were used for testing. P-SBPs4-Zn was dissolved in MEM medium at concentrations of 0, 0.25, 0.5, 0.75, 1, and 1.25 mg/mL. Caco-2 cells were diluted and seeded at a density of 10,000 cells per well in a 96-well plate, then cultured in a 37 °C, 5 % CO_2 incubator. After 24 h of culture, cells were treated with the different concentrations of sample. After 24 h, 5 mg/mL MTT dye was added and incubated at 37 °C for 4 h. The medium was replaced with 150 μL dimethyl sulfoxide (DMSO) to dissolve the MTT, and the absorbance was measured at 570 nm.

2.13. Statistics analysis

Experimental data were measured at least 3 times in all tests ($n \geq 3$). Origin 2021 software was used for mapping. The univariate ANOVA test was conducted using IBM SPSS Statistics 27 software, followed by *post hoc* comparisons using the Waller-Duncan test. Differences were considered statistically significant at $P < 0.05$.

3. Results and discussion

3.1. Molecular weight distribution analysis

The molecular weight distribution of peptides is crucial for their metal chelating capability, with low-molecular-weight peptides generally exhibiting stronger ability of metal chelation. Liu et al. (2013) reported that peptides with molecular weights of <2000 Da are particularly effective at chelating metal ions. In this study, approximately 50.25 % of SBPs had molecular weights of <3000 Da, indicating a high proportion of smaller peptides and suggesting a strong potential for zinc chelation (Fig. 1A).

3.2. Structural characteristics of P-SBPs at different pH values

3.2.1. FT-IR analysis

The FT-IR spectra of P-SBPs at various pH levels revealed substantial changes compared to those of SBPs (Fig. 1B). Following phosphorylation, the characteristic absorption peak at 3424 cm^{-1} (attributed to -N-H stretching) shifted to approximately 3473 cm^{-1} (Kaewruang et al., 2014), while the amide I peak at 1630 cm^{-1} displayed a blue shift. No marked changes were observed in amide II (1544 cm^{-1}) and amide III (1243 cm^{-1}) bands, indicating minimal involvement of the C═O and C—N groups in phosphorylation. A distinct peak around 890 cm^{-1}, corresponding to P—O stretching vibrations, confirmed the successful incorporation of sodium tripolyphosphate with SBPs, aligning with findings from previous studies.

3.2.2. CD spectral analysis

The CD spectra of SBPs in Fig. 1C illustrate substantial structural changes in SBPs following phosphorylation. The addition of phosphate groups caused blue shift in the absorption peaks of P-SBPs within the 190–210 nm range, varying across pH levels. Notably, phosphorylation altered the secondary structure composition of P-SBPs-Zn, where random coil content increased by 1.19 % and β-sheet content decreased by 1.12 % (Fig. 1D). The α-helix and β-turn proportions in P-SBPs4-Zn remained relatively stable. This structural shift from β-sheet to random coil suggests that the addition of phosphoryl groups introduces hydrogen bonds between the phosphate groups and peptide backbones. These new bonds likely weaken the existing intermolecular hydrogen bonding, particularly between amide hydrogens and carbonyl oxygens), resulting in structural interconversions and possibly refolding or unfolding of the peptide molecules. This finding agrees with the study by Geng et al. (2014), who observed similar secondary structure adjustments due to phosphorylation.

3.2.3. Fluorescence spectroscopy

Fig. 1E illustrates the fluorescence intensity trends at 360 nm under 290 nm excitation. Notably, the fluorescence intensity of P-SBPs at various pH levels was significantly lower than that of unphosphorylated SBPs, consistent with previous findings (Li et al., 2010). Among the tested pH levels, the P-SBPs4 exhibited the highest fluorescence intensity. This reduction in fluorescence intensity may result from structural modifications to the peptide, which exposed the chromophore to a

more polar environment (Sheng et al., 2017). Phosphorylation also induces conformational modifications that enhance the exposure of tryptophan (Trp) residues, causing a slight blue shift in fluorescence. These observations suggest notable structural distinctions between phosphorylated and unphosphorylated peptides.

3.2.4. H_0 analysis

The H_0 index for P-SBPs at different pH levels is presented in Fig. 1F. Compared with SBPs, the H_0 index of P-SBP4 was significantly elevated, indicating increased surface hydrophobicity and decreased solubility. This change likely arose from the exposure of hydrophobic tryptophan and tyrosine groups on the surface of P-SBPs4 particles, thereby reducing UV absorption and amplifying surface hydrophobicity. These findings are consistent with previous reports, showing that phosphorylation tends to increase protein residue hydrophobicity relative to non-phosphorylated peptides (Li et al., 2010). Specifically, when positively

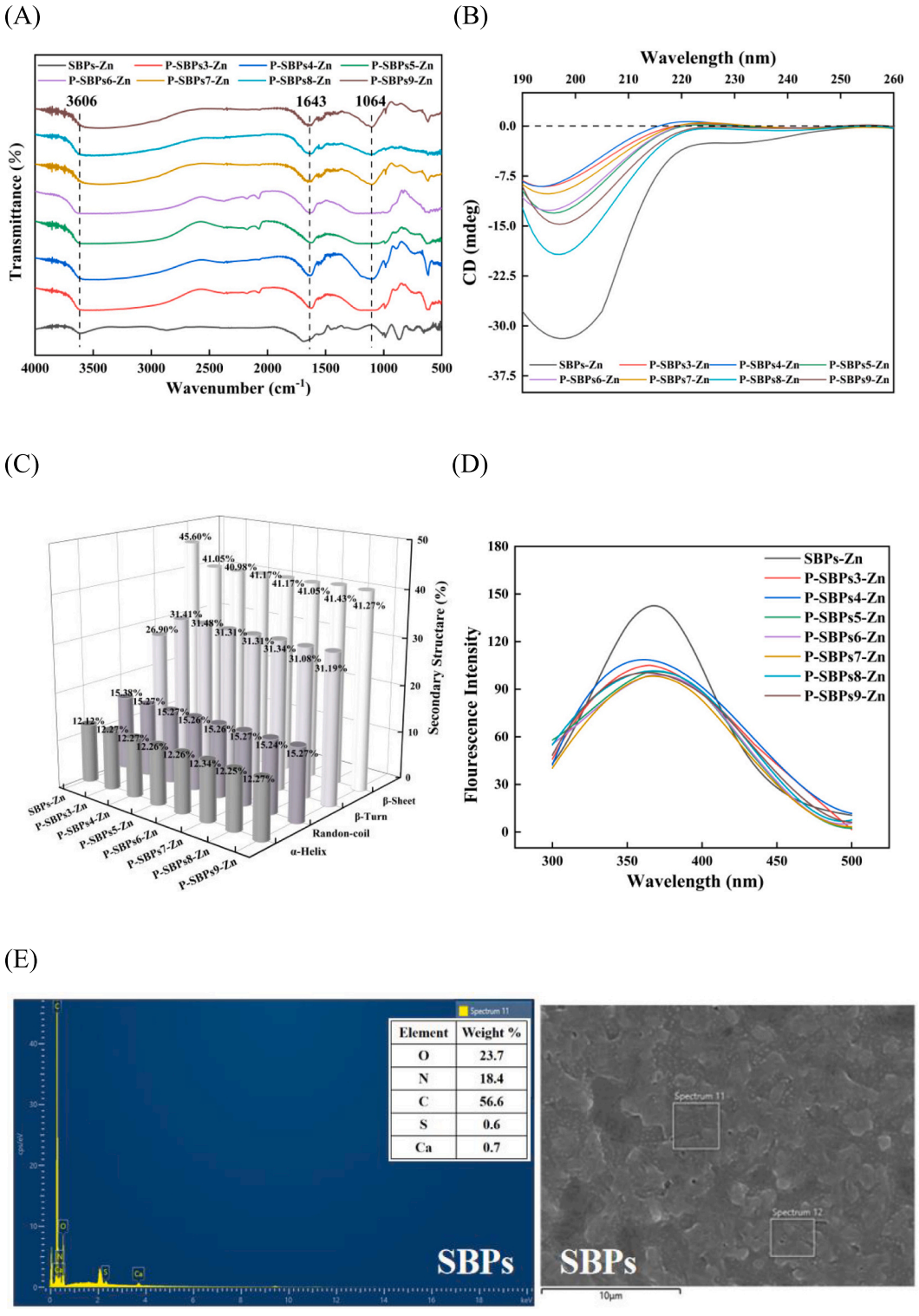

Fig. 2. The structure of P-SBPs-Zn at different pH values. (A) FT-IR; (B) circular dichroism spectrum; (C) secondary structure distribution; (D) fluorescence spectrum. Surface element composition and microstructure. (E) SBPs; (F) P-SBPs4; and (G) P-SBPs4-Zn.

(F)

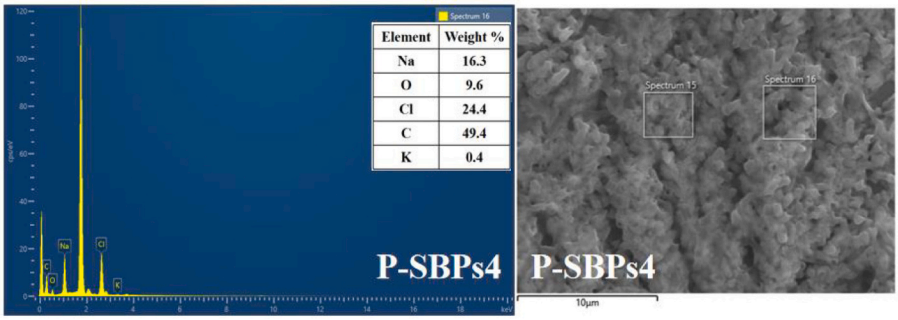

(G)

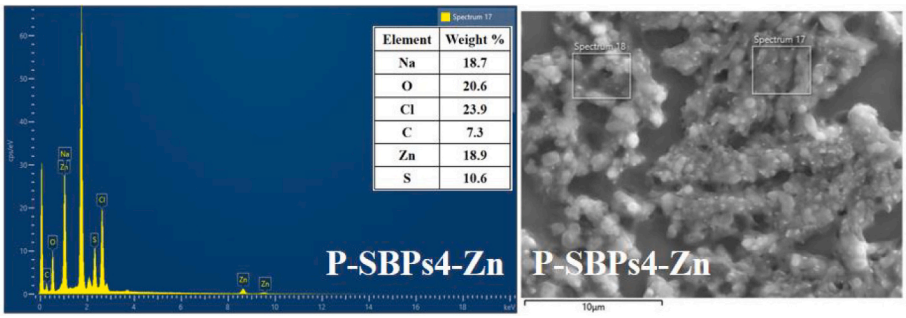

Fig. 2. (*continued*).

charged, zinc ions interact with specific peptide chain residues, forming salt bridges through electrostatic attraction. Furthermore, the side chains of some residues may engage in hydrogen bond formation, further diminishing the hydrophilicity of these residues and highlighting the hydrophobicity of other side chains. Therefore, the relative increase in the number of hydrophobic groups in the peptide chain significantly enhances the hydrophobicity of the entire molecular surface. This shift in hydrophobic groups may have a profound impact on the structure and function of the peptide chain.

3.3. Structural characteristics of P-SBPs-Zn at different pH values

3.3.1. Analysis of phosphorylation degree and zinc chelating ability

Following the phosphorylation reaction of SBPs, as depicted in Fig. 1G, the phosphorus content of the modified SBPs varied significantly across pH levels ($P < 0.05$). The phosphorus content of unmodified SBPs was (0.23 ± 0.01) mmol/L, whereas the highest phosphorus content was observed in P-SBPs4 as (1.27 ± 0.02) mmol/L among different pH values, indicating successful phosphorylation and a substantial increase in phosphorus content. Variations in the degree of phosphorylation could be attributed to differences in raw materials and reaction processes, which affect the phosphorylation sites (Sheng et al., 2019). Studies have demonstrated that phosphate groups can be attached to oxygen atoms in serine, threonine, aspartic acid (β-carboxylic acid), and tyrosine residues, or through nitrogen in lysine (ε-amino) and histidine (1 and 3) residues (Zhang et al., 2007). Xiong and Ma (2017) and Wang et al. (2016) reported that most phosphorylation sites in ovalbumin are located on serine residues. The zinc chelation capacity of the phosphorylated peptides is depicted in Fig. 1H. P-SBPs4 exhibited the highest zinc content, measuring (86.15 ± 0.47) mg/g ($P < 0.05$). These aforementioned results indicate that the zinc chelating ability of P-SBPs varies significantly depending on the different pH levels, with P-SBPs4 displaying optimal zinc-binding properties.

3.3.2. FT-IR analysis

As shown in Fig. 2A, the most significant change after zinc chelation is the marked shift of the absorption band from 1078 cm^{-1} to 1064 cm^{-1}. This absorption band is unequivocally attributed to the P—O stretching vibration of the phosphate group introduced by phosphonation. This shift toward lower wavenumbers is a classic signature of phosphate oxygen atoms participating in metal coordination. Upon forming the P—O—Zn bond with zinc, the vibrational system gains mass while the P—O bond constant weakens, leading to the observed red shift. Additionally, we observed a subtle yet stable shift in the band near 1636 cm^{-1} (amide I, C═O stretching vibration), ultimately stabilizing at 1643 cm^{-1}. This provides strong direct evidence that the phosphate group serves as the primary binding site for Zn^{2+}.

3.3.3. CD spectral analysis

The secondary structure distribution was analyzed using CDNN based on the molecular weight distribution. The molecular weight distribution of P-SBPs at different pH values is shown in Supplementary Fig. 2A. The molecular weight distribution of P-SBPs-Zn at different pH values is shown in Supplementary Fig. 2B. In the CD spectra of P-SBPs-Zn at different pHs, a prominent negative peak appeared at about 195 nm, indicating that the secondary structure of P-SBPs at different pHs changed significantly during the chelation process (Fig. 2B). Compared with SBPs-Zn, the α-helix content in P-SBPs4-Zn increased by 4.62 %, whereas the content of random coil structures decreased by 4.58 % (Fig. 2C). This shift may be attributed to zinc-induced peptide self-assembly, which favored α-helix and random coil structures. These findings are consistent with those of Li et al. (2010).

3.3.4. Fluorescence spectroscopy

Although the amide carbonyl group itself exhibits weak metal-binding capacity, the side-chain carboxyl groups of aspartic acid (Asp) and glutamic acid (Glu) residues in salmon bone peptides absorb in a similar wavelength range. This shift suggests the carboxyl groups may participate in coordination interactions, a hypothesis further supported

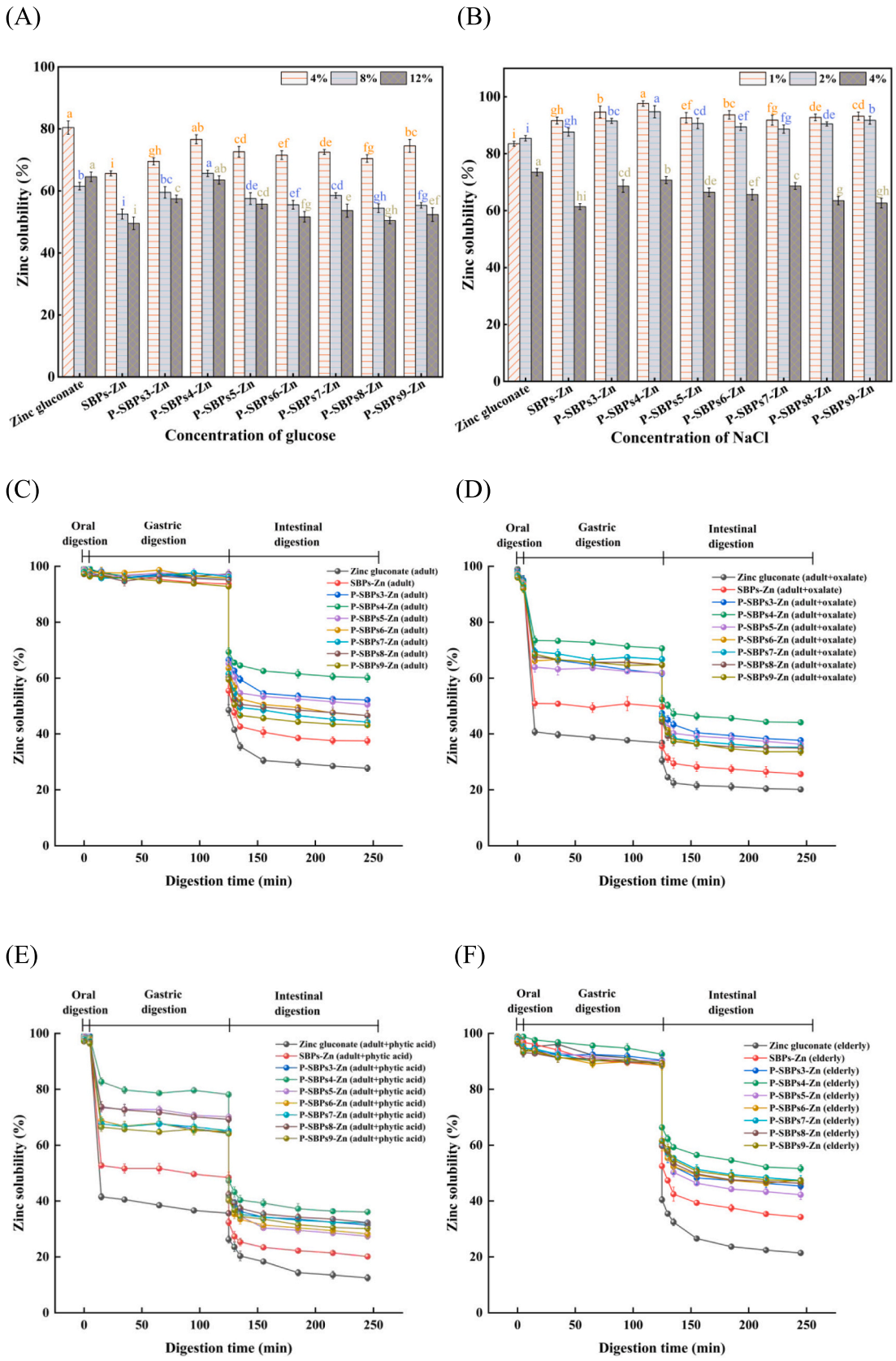

Fig. 3. The stability of P-SBPs-Zn at different pH values. (A) With addition of different concentrations of glucose (4–12 g/100 g); (B) With addition of different concentrations of NaCl (1–4 g/10 g) ($P < 0.05$, different colors represent different groups); (C) simulated digestion in adults; (D) simulated digestion with oxalic acid in adults; (E) simulated digestion with phytic acid in adults; (F) simulated digestion in elderly people; (G) simulated digestion with oxalic acid in elderly people; and (H) simulated digestion with phytic acid in elderly people.

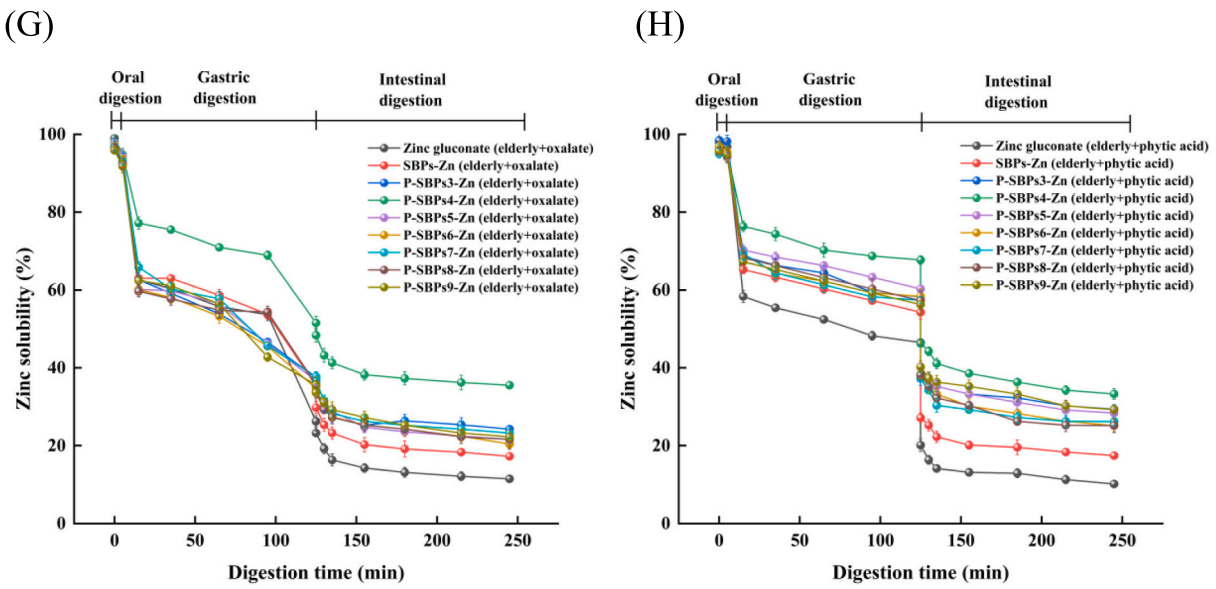

Fig. 3. (*continued*).

by fluorescence spectroscopy results (Fig. 2D). The endogenous fluorescence quenching observed upon zinc ion addition (primarily originating from tyrosine and tryptophan residues) indicates that the coordination environment alters the microenvironment of these luminescent groups. This is consistent with a binding event inducing conformational changes, a process that may bring residues containing carboxyl groups into proximity with aromatic amino acids.

3.3.5. *Elemental composition*

Fig. 2E, F and G show the elemental differences between SBPs, P-SBPs4 and P-SBPs4-Zn, respectively. SBPs primarily consisted of C (56.6 %), N (18.4 %), O (23.7 %), S (0.6 %) and Ca (0.7 %). In P-SBPs, the elemental composition shifted to Na (17.3 %), O (9.4 %), Cl (26.7 %), and C (46.6 %). The P-SBPs4-Zn composition further altered to Na (18.7 %), O (20.6 %), Cl (23.9 %), C (7.3 %), Zn (18.9 %), and S (10.6 %), clearly indicating successful zinc chelation. SEM imaging revealed substantial morphological differences: SBPs displayed a smooth planar surface, whereas P-SBPs4 formed relatively aggregated particles. In P-SBPs4-Zn, the surface appeared as more aggregated clusters of globular particles, likely due to interactions between zinc ions and the peptide, forming stable P-SBPs4-Zn complexes. White dots on the surface of the P-SBPs4-Zn complex suggest zinc ion binding (Zhang et al., 2018). Moreover, the observed folding and crystal structures may stem from peptide–zinc ion interactions. This structural modification is consistent with Sun et al. (2021), supporting the notion that zinc chelation enhances the peptide's microstructure, forming densely packed nanoparticles.

3.4. *Stability analysis of P-SBPs-NP-Zn at different pH values*

3.4.1. *Effects of glucose and NaCl treatments*

Excess sodium ions and glucose can influence zinc ion absorption in the body (Khan et al., 2022). Fig. 3A and B demonstrate that adding glucose (8 %–12 %, *w*/w) or a high NaCl concentration (4 %) significantly reduced ($P < 0.05$) zinc solubility in P-SBPs-Zn and zinc gluconate. As shown in Fig. 3A. When 4 % glucose was added, the zinc solubility of zinc gluconate was (80.42 ± 2.14) %, and it was (64.55 ± 1.53) % when the glucose concentration rose to 12 %. The zinc solubility of P-SBPs4-Zn decreased from (76.65 ± 1.44) % to (63.54 ± 1.32) %. The zinc solubility of P-SBPs-Zn is the highest when the pH value is 4, and it is the most stable under the condition of adding different concentrations of glucose. Adding low NaCl concentrations (1 %–2 %) did not significantly result in the same changes ($P > 0.05$). As shown in Fig. 3B. When the NaCl concentration was added from 1 % to 4 %, the zinc solubility of zinc gluconate decreased from (83.53 ± 0.86) % to (73.52 ± 1.28) %. The zinc solubility of P-SBPs4-Zn decreased from (97.64 ± 0.97) % to (70.75 ± 1.21) %. These results suggest that P-SBPs-Zn is stable at low NaCl concentrations (1–2 %), but unstable in the presence of glucose (8 %–12 %) and higher NaCl concentrations (4 %). Numerous sodium ions or glucose molecules can change the polarity of the microenvironment around the peptide, which affects the peptide–zinc ion interaction, leading to reduced zinc solubility (Wong et al., 2019). Additionally, zinc solubility in P-SBPs-Zn under NaCl treatments at various pH levels was higher than that in zinc gluconate, with P-SBPs4-Zn exhibiting the highest solubility. This result suggests that phosphorylation-enhanced zinc chelation improves the stability of zinc ions at low glucose and NaCl concentrations, potentially enhancing zinc bioavailability.

3.4.2. *Simulated gastrointestinal digestion in adults*

In Fig. 3C, the solubility of P-SBPs-Zn at different pH values decreased significantly ($P < 0.05$) as the simulated digestion progressed from the oral phase (0–5 min) to the gastric phase (5–125 min) and then into the intestinal phase (125–245 min). This trend is similar to that observed in zinc gluconate. When zinc ions transition from the stomach to the intestines, some Zn^{2+} ions convert into insoluble zinc salts because of the increased pH (Udechukwu et al., 2018). Additionally, during gastrointestinal digestion, the peptide chain (P-SBPs) may degrade, weakening the interaction between peptides and zinc ions, which further reduces zinc solubility. This process presents a barrier that zinc supplements must overcome to achieve physiological efficacy in the body (Wang et al., 2018). Among the different pH levels, the zinc solubility of P-SBPs-Zn was significantly higher than that of zinc gluconate ($P < 0.05$), with P-SBPs4-Zn demonstrating the highest zinc solubility at the end of process, achieving (60.13 ± 1.56) %, confirming its improved stability under intestinal digestion conditions. Similar trends have been reported previously (Sun et al., 2021). Hence, these findings suggest that P-SBPs4-Zn enhances zinc stability in intestinal environments.

Fig. 3D and E further illustrate that during simulated gastric digestion with food components, whose interaction with zinc ions led to a decrease in zinc solubility due to precipitation. In the simulated intestinal environment, the alkaline conditions foster the formation of Zn $(OH)_2$ as OH^-, oxalate, and phytic acid compete with zinc ions, further reducing zinc solubility. In systems supplemented with oxalic acid and

phytic acid, the final solubility of P-SBPs4-Zn reached its maximum values at the end of digestion, at (44.14 ± 0.35) % and (36.11 ± 0.93) %, respectively. Oxalate, commonly found in foods, can significantly hinder zinc absorption by forming insoluble precipitates, which the human body cannot absorb effectively (Wang et al., 2024). Phytic acid, present mainly in grains, beans, and other plants, can inhibit mineral absorption and form insoluble and indigestible phytomineral complexes in the intestine (Wang et al., 2023). P-SBPs4-Zn shows an improved ability to prevent the formation of insoluble zinc complexes in the intestines, thereby enhancing zinc bioavailability.

Notably, the presence of calcium ions (Ca^{2+}) enhances phytic acid's inhibition of zinc absorption by forming insoluble calcium-phytic acid-zinc complexes (Christensen et al., 2025). Consequently, the (phytic acid × calcium): zinc molar ratio has been identified as ations, the synergistic interaction between calcium and phytic acid may pose greater challenges to the stability of zinc-peptide complexes. Consequently, future studies should employ more complex *in vitro* gastrointestinal models incorporating calcium ions, or ultimately conduct *in vivo* experiments, to comprehensively evaluate the bioavailability of P-SBPs4-Zn in real food matrices and validate its efficacy as a zinc fortifier.

3.4.3. Simulated gastrointestinal digestion in elderly people

Fig. 3F shows the stability of *in vitro* simulated gastrointestinal digestion in older adults Zinc solubility of the zinc chelates was significantly lower in the elderly digestion model compared to the adult one. This reduced solubility may stem from decreased gastric acid secretion and lower pepsin activity in elderly individuals, influenced by changes in gastric pH. Despite this, P-SBPs4-Zn retained the highest digestibility, with a zinc solubility of (51.63 ± 1.35) % at the end of digestion (Fig. 3F). Fig. 3G and H depict the effects of oxalic acid and phytic acid in the elderly digestion model, respectively, showing trends consistent with the adult model: reduced pepsin and bile concentrations lead to poorer digestion, resulting in impaired protein breakdown and reduced zinc bioavailability (Wang et al., 2022). At the end of digestion, in the presence of oxalic acid and phytic acid, P-SBPs4-Zn displayed the highest zinc solubility of (35.54 ± 0.96) % and (33.27 ± 1.36) %,

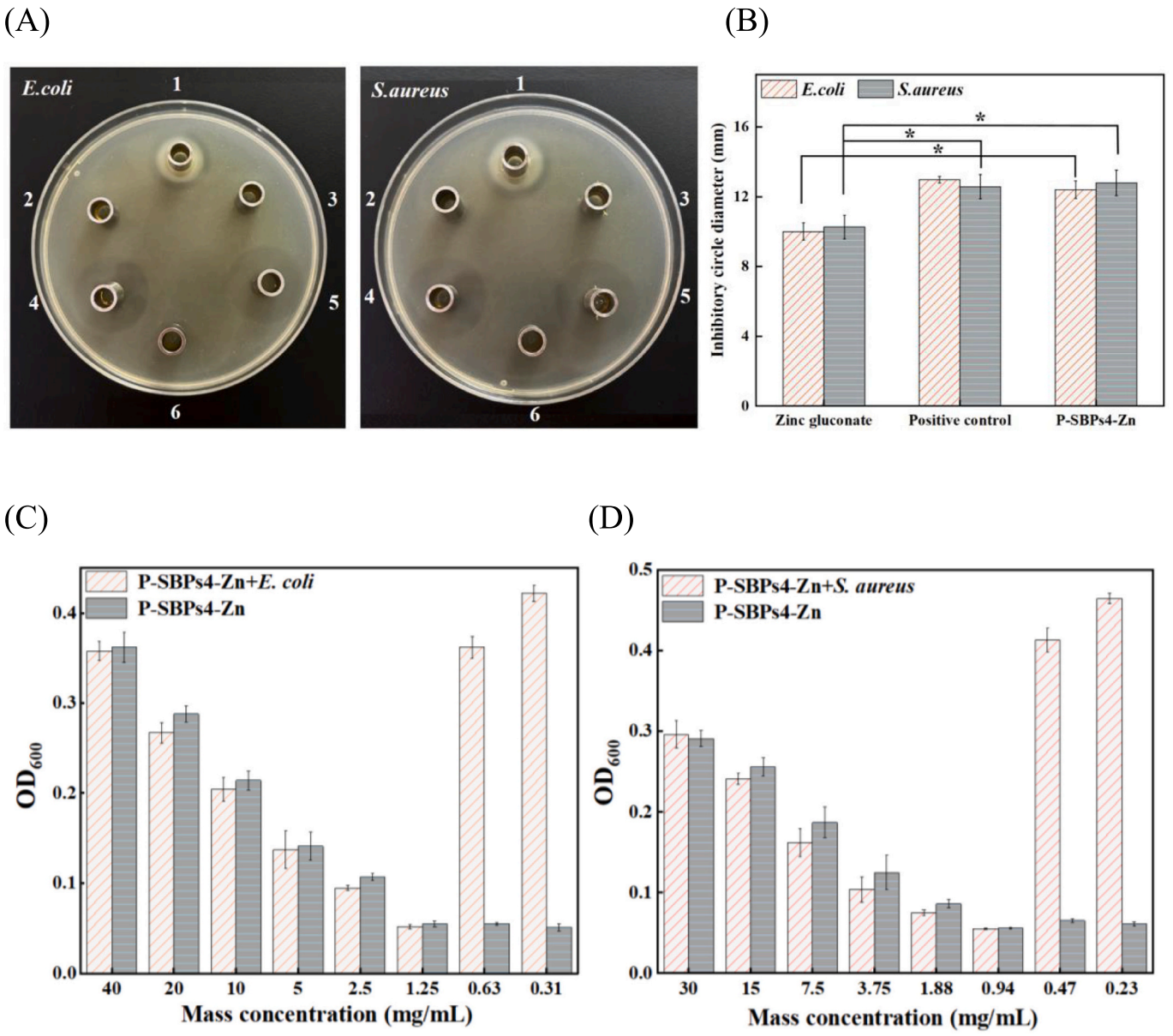

Fig. 4. Antibacterial activity of P-SBPs4-Zn. (A) Oxford cup diffusion test: 1. Zinc gluconate, 2. Sterile water, 3. SBPs (100 mg/mL), 4. 0.2 % streptomycin/potassium sorbate; 5. P-SBPs4-Zn (100 mg/mL), 6. P-SBPs4 (100 mg/mL); (B) circle of inhibition diameters of zinc gluconate, positive control and P-SBPs4-Zn; minimum inhibitory concentrations (MIC) of P-SBPs4-Zn against (C) *E. coli* and (D) *S. aureus*. (*$P < 0.05$).

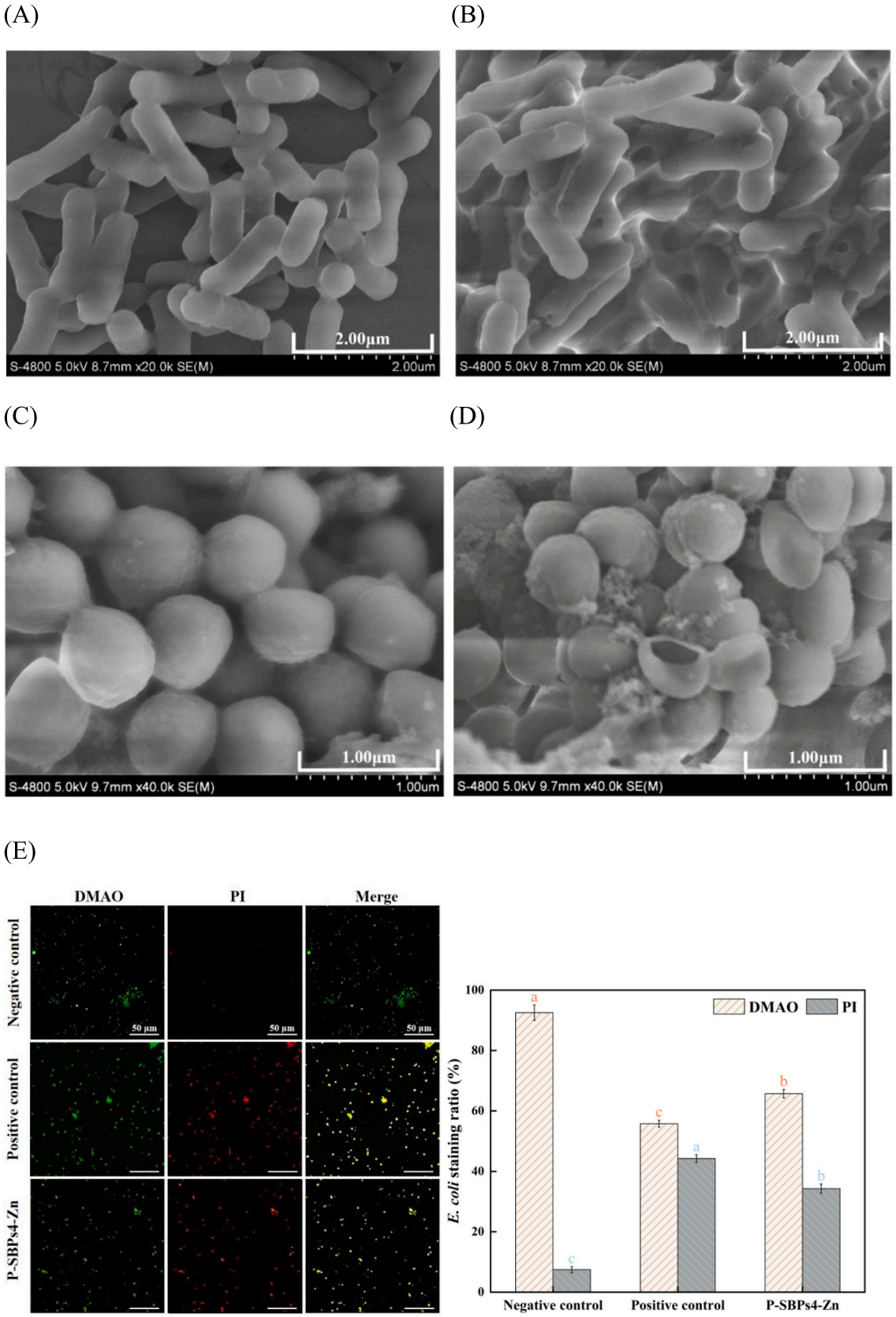

Fig. 5. Scanning electron microscopy image of *E. coli*. (A) Untreated cells; (B) P-SBPs4-Zn-treated cells. Scanning electron microscopy image of *S. aureus*. (C) Untreated cells; (D) P-SBPs4-Zn-treated cells; (E) results of double staining of *E. coli* by DMAO/PI and the percentage of staining; (F) results of double staining of *S. aureus* by DMAO/PI and percentage of staining ($P < 0.05$, different colors represent different groups).

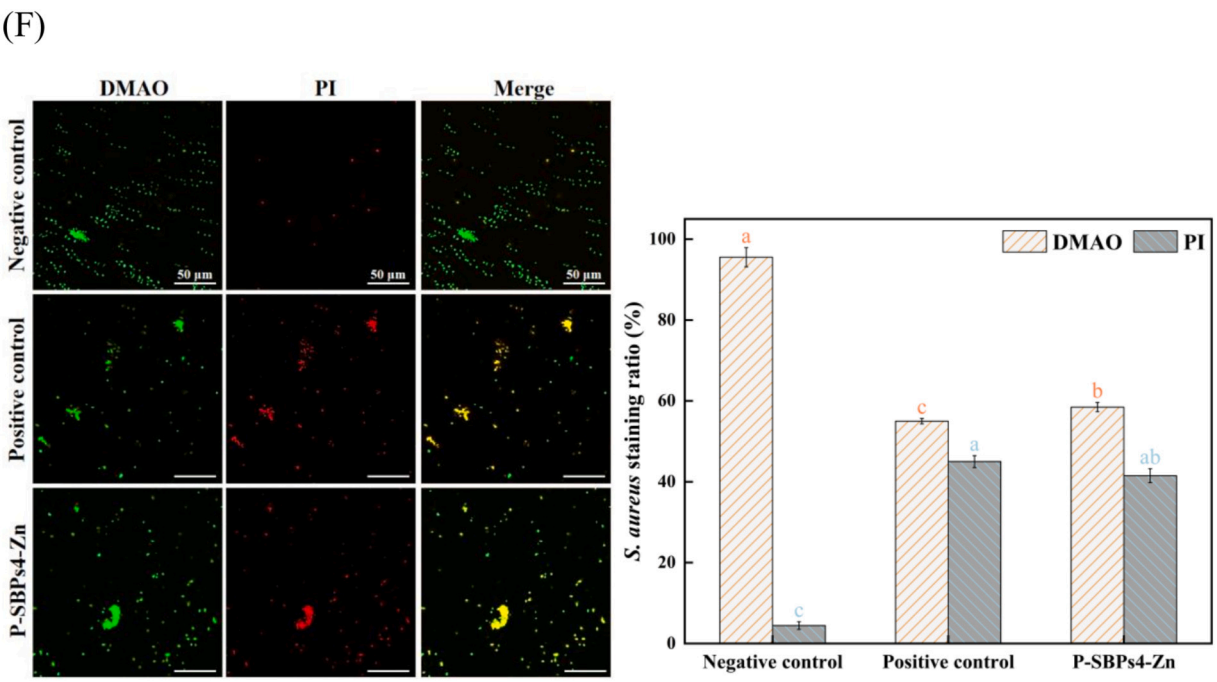

Fig. 5. (*continued*).

respectively. Therefore, P-SBPs-Zn chelates at varying pH values demonstrated a buffering effect, while P-SBPs4-Zn exhibited the strongest resilience to digestive enzymes and alkaline conditions, making it an effective zinc supplement.

3.5. Antibacterial activity assay

The antibacterial activity of P-SBPs4-Zn was evaluated against *E. coli* and *S. aureus*. In Fig. 4A and B, the inhibition zone diameter of P-SBPs4-Zn for *E. coli* was (12.4 ± 0.50) mm, exceeding that of zinc gluconate with equivalent zinc concentrations (10.0 ± 0.49) mm, calculated by measuring the chelation rate with EDTA titration). Similarly, the inhibition zone diameter of P-SBPs4-Zn against *S. aureus* was (12.8 ± 0.74) mm, also outperforming zinc gluconate (10.27 ± 0.67) mm, which contained the same zinc concentration as P-SBPs4-Zn. Three parallel Oxford cup circle of inhibition experiments are shown in Supplementary Fig. 3. The ability to inhibit both bacteria was second only to the positive control. These results indicate that zinc ions chelated with P-SBPs4 exhibit improved antibacterial effects against both gram-positive and gram-negative bacteria compared to zinc gluconate. The positive controls, streptomycin and potassium sorbate, produced inhibition zones of (12.97 ± 0.19) mm and (12.57 ± 0.69) mm, respectively. Thus, P-SBPs4-Zn demonstrated effective antibacterial activity for both bacterial types.

The MIC of P-SBPs4-Zn against *E. coli* and *S. aureus* was determined using the microdilution method. As shown in Fig. 4C and D, 1.25 mg/mL was the lowest P-SBPs4-Zn concentration to inhibit *E. coli* growth, and 0.94 mg/mL was the lowest P-SBPs4-Zn concentration to inhibit *S. aureus*. The MIC values of P-SBPs4-Zn were lower compared to Fang et al. (2019) and showed commercially viable antimicrobial potency in the context of food preservation.

3.6. Scanning electron microscopy

SEM was used to observe morphological changes in *E. coli* and *S. aureus* after treatment with P-SBPs4-Zn. Untreated *E. coli* displayed a typical rod-like shape, uniform size, and smooth, intact cell surfaces (Fig. 5A). However, *E. coli* treated with P-SBPs4-Zn exhibited irregular shapes, wrinkled and rough surfaces, and signs of membrane disruption (Fig. 5B). Similarly, untreated *S. aureus* cells appeared spherical with smooth, intact surfaces (Fig. 5C), whereas P-SBPs4-Zn-treated *S. aureus* cells became irregular, wrinkled, and adhered to each other, with some cells ruptured (Fig. 5D). These findings confirm that P-SBPs4-Zn exerted a significant inhibitory effect on *E. coli* and *S. aureus* by disrupting their cell membranes, likely causing death. This observation is consistent with the experimental results of antimicrobial activity. P-SBPs4-Zn thus can inhibit both gram-positive and gram-negative bacteria.

3.7. Cell membrane integrity

The difference in fluorescence staining between live and dead bacteria can be observed very clearly after double staining of *E. coli* and *S. aureus* using DMAO and PI double staining superimposed (Merge). The results of cell staining can be observed under confocal laser scanning microscope (CLSM) and the proportion of organisms stained with the two dyes can be counted. As seen in Fig. 5E and F, the negative control group showed basically green fluorescence after the superposition of the two fluorescence signals, and the yellow fluorescence was basically missing or only individually visible. In the positive control and P-SBPs4-Zn groups, the number of red and green fluorescence staining was basically the same, and the two fluorescence types were almost completely overlapped, where yellow fluorescence was seen after superposition. The proportion of *E. coli* treated with P-SBPs4-Zn and stained by PI was (34.39 ± 1.52) % (Figs. 5E), and the proportion of *S. aureus* was (41.52 ± 1.73) % (Figs. 5F). The red fluorescence was mainly concentrated in the nucleus, *i.e.* P-SBPs4-Zn disrupted the integrity of the cell membrane and led to the death of some bacteria. The percentage of PI-stained positive controls was (44.22 ± 1.25) % for *E. coli* (Figs. 5E) and (45.01 ± 1.47) % for *S. aureus* (Figs. 5F). The P-SBPs4-Zn group was second only to the positive control group. The above results indicated that P-SBPs4-Zn was able to disrupt the cell membrane integrity of both Gram-negative and Gram-positive bacteria.

3.8. Nucleic acid and protein leakage

Nucleic acids (OD_{260nm}) and proteins released from *E. coli* and

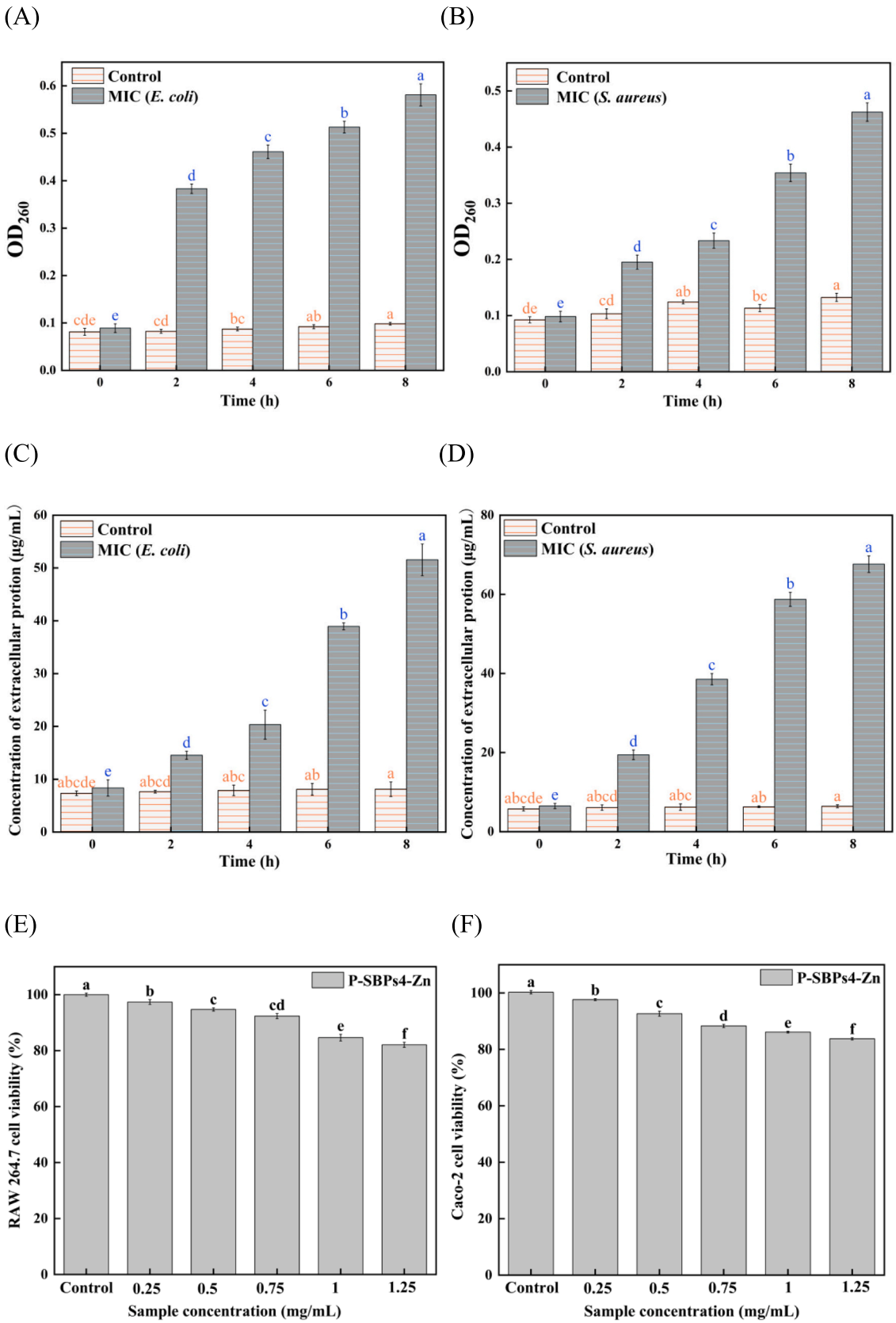

Fig. 6. Effect of P-SBPs4-Zn on cell membrane integrity of *E. coli* and *S. aureus*. (A) nucleic acid leakage in *E. coli;* (B) nucleic acid leakage in *S. aureus;* (C) protein leakage in *E. coli.*; (D) protein leakage in *S. aureus*. Biosafety evaluation of P-SBPs4-Zn. (E) RAW 264.7 cell; (F) Caco-2 cell. ($P < 0.05$, different colors represent different groups).

S. aureus in the supernatant after P-SBPs4-Zn treatment were measured as indicators of membrane disruption. The results in Fig. 6A and B showed that nucleic acid release increased significantly with time, indicating cell membrane damage. 8 h later, the absorbance value (OD_{260nm}) of nucleic acids increased from 0.09 to 0.58 in *E. coli* (OD_{260nm}) and from 0.09 to 0.46 in *S. aureus* (OD_{260nm}). From 0 to 8 h, the protein release from *E. coli* increased significantly from (8.34 ± 1.54) μg/mL to (51.54 ± 2.99) μg/mL (Fig. 6C). The protein release from *S. aureus* increased significantly from (6.5 ± 0.65) μg/mL to (67.63 ± 2.1) μg/mL (Fig. 6D). These results confirmed that P-SBPs4-Zn irreplaceably disrupted the bacterial cell membrane, leading to the leakage of intracellular components and ultimately cell death. This observation is consistent with the SEM and CLSM results.

3.9. Biosafety of P-SBPs4-Zn

3.9.1. RAW 264.7 cells

The potential cytotoxicity of P-SBPs4-Zn was evaluated using RAW 264.7 cell and MTT assays. As shown in Fig. 6, cell viability was (97.38 ± 0.86) % for 0.25 mg/mL of P-SBPs4-Zn and (82.09 ± 0.90) % for 1.25 mg/mL. All the cell viability after treatment with different concentrations of P-SBPs4-Zn was greater than 80 % in the MTT assays, which typically indicates low cytotoxicity (Liu et al., 2024). Therefore, the zinc chelates of SBPs prepared by hydrolysis with water-soluble protease are suitable as a potential nutrient fortifier.

3.9.2. Caco-2 cells

Based on an assessment of the substance's impact on intestinal epithelial cell survival rates, the safety of P-SBPs4-Zn was evaluated using the MTT assay. As shown in Fig. 6F, after treating Caco-2 cells with various concentrations of P-SBPs4-Zn for 24 h, cell viability exceeded 80 % in all cases. This indicates that P-SBPs4-Zn is safe and suitable as a potential nutritional fortifier.

4. Conclusions

In summary, peptides (SBPs) were extracted from salmon bones through enzymatic hydrolysis with neutral proteases, and their phosphorylated forms (P-SBPs) were prepared at different pH levels. After zinc ion chelation, the structural changes of P-SBPs-Zn at different pH values were characterized by infrared spectroscopy and fluorescence spectroscopy, and its zinc binding ability was evaluated. The antibacterial mechanism of the optimal form P-SBPs4-Zn was deeply studied. P-SBPs4-Zn has the best solubility and zinc chelating property, with a zinc content of 86.15 ± 0.47 mg/g. Functional groups (such as amino, hydroxyl and carboxyl groups) play an important role in the binding of Zn^{2+}. Furthermore, after the addition of food coexisting components, P-SBPs4-Zn remained stable at low glucose and NaCl concentrations as well as during simulated gastrointestinal digestion processes in adults and the elderly. The safety assessment using Caco-2 (intestinal epithelial cells) and RAW 264.7 (immune cells) cells confirmed its biocompatibility, supporting its suitability for oral application. SEM and CLSM observations revealed that P-SBPs4-Zn had a strong inhibitory effect on *E. coli* and *S. aureus* by destroying the bacterial cell membrane. The dual functions of P-SBPs-Zn as a zinc supplement and a mild preservative enhance its value proposition in functional food applications. By integrating these two roles, it reduces the need for additional preservatives, thereby lowering the overall formula cost while maintaining the product's efficacy. These research results provide innovative approaches for the effective utilization of Marine waste resources and highlight the potential application of Marine peptide zinc chelates as antibacterial agents in the food industry.

CRediT authorship contribution statement

Lingyu Han: Writing – review & editing, Writing – original draft, Methodology, Conceptualization. **Nuo Dong:** Writing – review & editing, Writing – original draft, Methodology, Conceptualization. **Bing Hu:** Methodology, Conceptualization, Formal analysis, Writing – review & editing. **Jixin Yang:** Writing – review & editing, Methodology, Conceptualization. **Zhiwei Jiao:** Software, Methodology, Conceptualization. **Kun Ma:** Software, Methodology, Conceptualization. **Zhe Xu:** Writing – review & editing, Software, Conceptualization. **Tingting Li:** Writing – review & editing, Writing – original draft, Methodology, Formal analysis, Conceptualization.

Declaration of competing interest

The authors declare that they have no known competing financial interests or personal relationships that could have appeared to influence the work reported in this paper.

Acknowledgements

This work was supported by the 14th Five-Year National Key Research and Development Plan Project (2024YFD2401605); Science and Technology Innovation Fund of Dalian (2023JJ11CG007).

Appendix A. Supplementary data

Supplementary data to this article can be found online at https://doi.org/10.1016/j.fochx.2025.103350.

Data availability

No data was used for the research described in the article.

References

Bajpai, V. K., Sharma, A., & Baek, K.-H. (2013). Antibacterial mode of action of Cudrania tricuspidata fruit essential oil, affecting membrane permeability and surface characteristics of food-borne pathogens. *Food Control, 32*(2), 582–590.

Chen, H., Lan, X., Guan, X., Luo, R., Zhang, Q., Ren, H., Xu, Z., & Tang, J. (2024). Comparative study on the effects of chitosan, carrageenan, and sodium alginate on the film-forming properties of fish skin gelatin. *LWT, 199*, Article 116111.

Christensen, B., Krüger, T. F., Hjorth, T. P., Buhl, E. H., & Sørensen, E. S. (2025). Milk osteopontin mediates zinc uptake in intestinal cells in the presence of phytic acid. *International Dairy Journal, 161*, Article 106113.

Diao, W. R., Hu, Q. P., Zhang, H., & Xu, J. G. (2014). Chemical composition, antibacterial activity and mechanism of action of essential oil from seeds of fennel (Foeniculum vulgare mill.). *Food Control, 35*(1), 109–116.

Fang, Z., Xu, L., Lin, Y., Cai, X., & Wang, S. (2019). The preservative potential of Octopus scraps peptides–zinc chelate against Staphylococcus aureus: Its fabrication, antibacterial activity and action mode. *Food Control, 98*, 24–33.

Feng, Y., Zhu, S., Yang, Y., Li, S., Zhao, Z., & Wu, H. (2024). Caseinophosphopeptides overcome calcium Phytate inhibition on zinc bioavailability by retaining zinc from Coprecipitation as zinc/ calcium Phytate Nanocomplexes. *Journal of Agricultural and Food Chemistry, 72*, 4757–4764.

Geng, X., Cui, B., Li, Y., Jin, W., An, Y., Zhou, B., Ye, T., He, L., Liang, H., Wang, L., Chen, Y., & Li, B. (2014). Preparation and characterization of ovalbumin and carboxymethyl cellulose conjugates via glycosylation. *Food Hydrocolloids, 37*, 86–92.

Han, L., Li, Y., Hu, B., Wang, W., Guo, J., Yang, J., Dong, N., Li, Y., & Li, T. (2024). Enhancement of calcium chelating activity in peptides from sea cucumber ovum through phosphorylation modification. *Foods, 13*(2), 1943.

Kaewruang, P., Benjakul, S., & Prodpran, T. (2014). Characteristics and gelling property of phosphorylated gelatin from the skin of unicorn leatherjacket. *Food Chemistry, 146*, 591–596.

Khan, S. T., Malik, A., Alwarthan, A., & Shaik, M. R. (2022). The enormity of the zinc deficiency problem and available solutions; an overview. *Arabian Journal of Chemistry, 15*(3), Article 103668.

Li, C. P., Chen, D., Peng, J., Enomoto, H., Hayashi, Y., Li, C., … Aoki, T. (2010). Improvement of functional properties of whey soy protein phosphorylated by dry-heating in the presence of pyrophosphate. *LWT - Food Science and Technology, 43*(6), 919–925.

Liu, F. R., Wang, L., Wang, R., & Chen, Z. X. (2013). Calcium-binding capacity of wheat germ protein hydrolysate and characterization of peptide–calcium complex. *Journal of Agricultural and Food Chemistry, 61*(31), 7537–7544.

Liu, Y., Ma, L., Guo, Y., Kuang, H., & Liu, Y. (2024). Fabricating oleic acid-ovalbumin complexes using an ultrasonic-coupled weakly alkaline pH technique: Improving the dispersibility, stability, and bioaccessibility of lutein in water. *Food Chemistry, 435*, Article 137593.

Luo, Y., Tu, Y., Ren, F., & Zhang, H. (2022). Characterization and functional properties of Maillard reaction products of β-lactoglobulin and polydextrose. *Food Chemistry, 377*, Article 131749.

Lv, F., Liang, H., Yuan, Q., & Li, C. (2011). *In vitro* antimicrobial effects and mechanism of action of selected plant essential oil combinations against four food-related microorganisms. *Food Research International, 44*(9), 3057–3064.

Ma, X., Nong, X.-H., Ren, Z., Wang, J., Liang, X., Wang, L., & Qi, S.-H. (2017). Antiviral peptides from marine gorgonian-derived fungus aspergillus sp. SCSIO 41501. *Tetrahedron Letters, 58*(12), 1151–1155.

Quan, C., Zhang, Z., Liang, P., Zheng, J., Wang, J., Hou, Y., & Tang, Q. (2019). Bioactive gel self-assembled from phosphorylate biomimetic peptide: A potential scaffold for enhanced osteogenesis. *International Journal of Biological Macromolecules, 121*, 1054–1060.

Salami, S. A., Oluwatosin, O. O., Oso, A. O., Fafiolu, A. O., Sogunle, O. M., Jegede, A. V., … Pirgozliev, V. (2016). Bioavailability of cu, Zn and Mn from mineral chelates or blends of inorganic salts in growing turkeys fed with supplemental riboflavin and/or pyridoxine. *Biological Trace Element Research, 173*(1), 168–176.

Sheng, L., Su, P., Han, K., Chen, J., Cao, A., Zhang, Z., Jin, Y., & Ma, M. (2017). Synthesis and structural characterization of lysozyme–pullulan conjugates obtained by the Maillard reaction. *Food Hydrocolloids, 71*, 1–7.

Sheng, L., Ye, S., Han, K., Zhu, G., Ma, M., & Cai, Z. (2019). Consequences of phosphorylation on the structural and foaming properties of ovalbumin under wet-heating conditions. *Food Hydrocolloids, 91*, 166–173.

Shi, C., Zhang, X., Zhao, X., Meng, R., Liu, Z., Chen, X., & Guo, N. (2017). Synergistic interactions of nisin in combination with cinnamaldehyde against Staphylococcus aureus in pasteurized milk. *Food Control, 71*, 10–16.

Sun, R., Liu, X., Yu, Y., Miao, J., Leng, K., & Gao, H. (2021). Preparation process optimization, structural characterization and *in vitro* digestion stability analysis of Antarctic krill (Euphausia superba) peptides-zinc chelate. *Food Chemistry, 340*, Article 128056.

Udechukwu, M. C., Collins, S. A., & Udenigwe, C. C. (2016). Prospects of enhancing dietary zinc bioavailability with food-derived zinc-chelating peptides. *Food & Function, 7*(10), 4137–4144.

Udechukwu, M. C., Downey, B., & Udenigwe, C. C. (2018). Influence of structural and surface properties of whey-derived peptides on zinc-chelating capacity, and *in vitro* gastric stability and bioaccessibility of the zinc-peptide complexes. *Food Chemistry, 240*, 1227–1232.

Wang, C., Li, B., & Ao, J. (2012). Separation and identification of zinc-chelating peptides from sesame protein hydrolysate using IMAC-Zn2+ and LC–MS/MS. *Food Chemistry, 134*(2), 1231–1238.

Wang, C., Zhao, F., Bai, Y., Li, C., Xu, X., Kristiansen, K., & Zhou, G. (2022). *In vitro* digestion mimicking conditions in young and elderly reveals marked differences between profiles and potential bioactivity of peptides from meat and soy proteins. *Food Research International, 157*, Article 111215.

Wang, L., Zhang, J., Yuan, Q., Xie, H., Shi, J., & Ju, X. (2016). Separation and purification of an anti-tumor peptide from rapeseed (Brassica campestris L.) and the effect on cell apoptosis. *Food & Function, 7*(5), 2239–2248.

Wang, Y., Bai, H., Wang, S., Wang, R., & Wang, Z. (2023). Casein phosphopeptide-calcium chelate: Preparation, calcium holding capacity and simulated digestion *in vitro*. *Food Chemistry, 401*, Article 134218.

Wang, Y., Wang, R., Bai, H., Wang, S., Liu, T., Zhang, X., & Wang, Z. (2024). Casein phosphopeptide calcium chelation: Preparation optimization, *in vitro* gastrointestinal simulated digestion, and peptide fragment exploration. *Journal of the Science of Food and Agriculture, 104*(2), 788–796.

Wang, Y. A., Liu, T., & Zhong, G. Q. (2019). Synthesis, characterization and applications of copper (II) complexes with Schiff bases derived from chitooligosaccharide and iodosubstituted salicylaldehyde. *Carbohydrate Polymers, 224*, Article 115151.

Wong, F.-C., Xiao, J., Ong, M. G. L., Pang, M.-J., Wong, S.-J., Teh, L.-K., & Chai, T.-T. (2019). Identification and characterization of antioxidant peptides from hydrolysate of blue-spotted stingray and their stability against thermal, pH and simulated gastrointestinal digestion treatments. *Food Chemistry, 271*, 614–622.

Xiong, Z., & Ma, M. (2017). Enhanced ovalbumin stability at oil-water interface by phosphorylation and identification of phosphorylation site using MALDI-TOF mass spectrometry. *Colloids and Surfaces B: Biointerfaces, 153*, 253–262.

Xu, J.-G., Hu, Q.-P., Wang, X.-D., Luo, J.-Y., Liu, Y., & Tian, C.-R. (2010). Changes in the main nutrients, phytochemicals, and antioxidant activity in yellow corn grain during maturation. *Journal of Agricultural and Food Chemistry, 58*(9), 5751–5756.

Yu, X., Xing, S., & Tan, M. (2024). Green synthesis of Zn2+ nanocarriers from Auricularia auricula fermentation broth with excellent antioxidant activity. *Food Chemistry, 442*, Article 138386.

Zhang, K., Li, Y., & Ren, Y. (2007). Research on the phosphorylation of soy protein isolate with sodium tripoly phosphate. *Journal of Food Engineering, 79*(4), 1233–1237.

Zheng, Y., Guo, M., Cheng, C., Li, J., Li, Y., Hou, Z., & Ai, Y. (2023). Structural and physicochemical characteristics, stability, toxicity and antioxidant activity of peptide-zinc chelate from coconut cake globulin hydrolysates. *LWT, 173*.

Zhu, S., Zheng, Y., He, S., Su, D., Nag, A., Zeng, Q., & Yuan, Y. (2021). Novel Zn-binding peptide isolated from soy protein hydrolysates: Purification, structure, and digestion. *Journal of Agricultural and Food Chemistry, 69*(1), 483–490.